AIAA SciTech Forum
6-10 January 2020, Orlando, FL
AIAA Scitech 2020 Forum

10.2514/6.2020-1579

Mode F/S Wave Packet Interference and Acoustic-like Emissions in a Mach 8 Flow Over a Cone

Christopher Haley* and Xiaolin Zhong†
University of California, Los Angeles, CA, 90095, USA

Acoustic-like waves are observed emanating from the boundary layer of a Mach 8 slender blunt cone simulation with a relatively low enthalpy, $h_o = 597kJ/kg$, and a warm wall, $T_w/T_e = 4.95$. The acoustic-like wave emissions are qualitatively similar to those attributed to the supersonic mode. The supersonic mode responsible for those emission, however, are found in high-enthalpy cold wall flows with blunter nose radii, making their appearance here unexpected. Unsteady simulation are carried out using blowing-suction actuators at two different surface locations. Analysis of the temporal data and spectral data using FFT reveals that the emissions are the result of a constructive/destructive interference between a primary wave packet and a satellite wave packet. Linear stability analysis on the steady state simulation indicates that the phase velocity of the primary wave is consistent with an unstable mode S (Mack's second mode), and that the phase velocity of the satellite wave packet is consistent with a stable supersonic mode F. Constructive/destructive interference between the wave packets also appears to have a damping effect on disturbance growth in one of the unsteady simulations, which prevents it from growing larger downstream.

I. Introduction

This paper is an investigation of primary and satellite wave packet interference with acoustic-like emissions from the boundary layer of a slender hypersonic cone. While investigating the ability of surface roughness to attenuate Mack's second mode instability,[1] acoustic-like waves were observed emitting from the boundary layer in an unsteady simulation with no surface roughness. These acoustic-like rays are qualitatively similar to those seen by Knisely and Zhong[2–4] in their investigation of supersonic modes. Moreover, the unsteady simulation in question also exhibited an interesting interference pattern which is thought to be caused by the interference of dispersive primary and satellite wave packets. Primary and satellite wave packets were are also seen in Knisely and Zhong's[4] unsteady results. Despite the similarities of the observed phenomena, and the results of Knisely and Zhong the simulation conditions are very different. Based on this limited observation, the proposed explanation for the acoustic-like boundary layer emissions is a supersonic mode. And the proposed explanation for the interference pattern is due to the dispersive nature of the boundary layer where the primary wave packet, consisting of Mack's second mode, and the satellite wave packet, consisting of a supersonic mode, spread dispersively into one another creating an interference pattern.

Supersonic modes were first described from numerical investigations performed by Mack in 1984,[5] 1987,[6] and 1990,[7] and by Reshotko in 1991.[8] Mack showed there exists discrete neutral waves whose phase velocity caused the wave to propagate upstream supersonically relative to the flow at the boundary layer edge. In other words $c_r < 1 - 1/M_e$, where c_r is the nondimensional phase velocity and M_e is the Mach number at the boundary layer edge; this is also some times represented as $\bar{M}(y) > 1$, where $\bar{M}(y)$ is the relative Mach number as a function of boundary layer height, and c is the dimensional phase velocity,

$$\bar{M} = \frac{M(y) - c}{a(y)}. \tag{1}$$

Mack also showed that supersonic modes transfer energy away from the wall. In simulations this property is exhibited as acoustic-like emissions from the boundary layer into the freestream (or the shock layer as

*Graduate Research Assistant, Mechanical and Aerospace Engineering Department,.
†Professor, Mechanical and Aerospace Engineering Department, AIAA associate fellow

it pertains to this paper). The emissions are described as acoustic-like because they originate not from an acoustic wave but from discrete modes.[9] In Mack's 1987[6] numerical investigation he found unstable supersonic waves—the instability however was weaker that the second mode instability and thus considered more benign.

Recently, there has been a renewed interest in supersonic modes. Their presence in high-enthalpy impulse facilities such as Caltech's T5 shock tunnel motivated Bitter and Shepard's[10] to investigate unstable supersonic modes over cold walls. Their numerical investigation looked at high-enthalpy thermal nonequilibrium on a flat plate with wall-to-edge temperature ratios between 1 and 0.2 with a wall temperature of $300K$. They found that decreasing the wall-to-edge temperature ratio lead to unstable supersonic waves over a wider frequency band. They also characterized that an unstable discrete mode (like Mack's second mode instability) is likely to become supersonically unstable when the complex phase speed has to cross the slow acoustic branch cut. Their investigation also considered the supersonic modes contribution to the N-factor, which increased with increasing Reynolds number. Bitter and Shepard concluded that while it contributes significantly at higher levels, the supersonic mode did not contribute significantly at the levels transition is experimentally known to occur: Mack's second mode instability is still the dominate cause of transition in hypersonic boundary layers.

Mortensen[11] also recently investigated supersonic modes and the effect of nose bluntness. The study focused on high-enthalpy flows with chemical nonequilibrium around slender blunt cones with nose radii from 1.1mm (the nominally "sharp" reference case) to 284.8mm. The simulations modeled inflight vehicle temperatures, which maintain a nominally cool wall ($T_w = 460K$) and promotes Mack's second mode instability. Mortensen's findings show that increasing the nose radius not only promotes supersonic mode instability but also increases the severity of the instability, eventually dominating over the traditional second mode instability. Unlike in Bitter and Shepard's investigation, Mortensen's unstable supersonic mode is the primary contributer to the N-factor and would lead to transition for typical levels.

Knisely and Zhong[3,4] also did an extensive DNS study of high-enthalpy flows on slender blunt cones with cold walls and chemical nonequalibrium. They used both LST and unsteady DNS to investigate unstable supersonic modes. A notable result of theirs is that, while they were able to detect unstable supersonic modes with DNS in two cases, LST analysis could only detect the mode in one case and not the other. The cases were nominally the same (and similar to Bitter and Shepards), but differed primarily in freestream temperature ($T_\infty = 1500K$ and $1000K$). They reasoned this was due to modal interaction, and suggested a combined LST and DNS approach to study the supersonic mode. This result is of particular interest to the current discussion because while acoustic-like waves are apparent in the DNS results, they could not be found with LST. The reasons for which are discussed herein.

Knisely and Zhong's work, like Bitter and Shepard's also emphasized the importance of the relative sonic line, $\bar{M}(y_s) = 1$. Their work includes an update diagram of neutral modes in the large wavenumber limit to include neutral supersonic modes in which acoustic wave-like modulation ($\bar{M} < -1$), subsonic rope-like structures ($-1 < \bar{M} < 1$), and decaying Mach waves ($\bar{M} > 1$) are visualized. Their work also includes an extensive background on the supersonic mode.

On the theoretical front, Xuesong and Zhang[12] provide results of a high Mach jet flow that emits acoustic-like waves. The result is qualitatively similar to the unsteady DNS results of Knisely and Zhong and the unsteady results contained herein.

The present paper looks at a low-enthalpy flow around a slender blunt (nominally sharp, $r_n = 0.5mm$) cone with a warm wall and perfect gas assumptions. These conditions share some overlap with the published cases already discussed, such as the test article geometry, but differ significantly in the areas of wall temperature, flow enthalpy, and gas chemistry. As already mentioned, the case parameters were not chosen to specifically study supersonic modes or acoustic radiation from the boundary layer.

Hypersonic laminar-turbulent boundary layer transition is an important area of research. Transition to turbulence can increase surface heating by a factor of 4-10 which necessitates an outsized thermal protection strategies.[13] The goal of transition research is to study the unsteady boundary layer, understand the mechanisms behind its behavior, and to reliably predict transition. The supersonic mode and second mode interference pattern are just one aspect of understanding hypersonic boundary layer behavior. It is important to know under what conditions the supersonic mode appears and its physical mechanism.

II. Governing Equation and Computational Methodology

The DNS code utilized in this paper is a 5^{th}-order accurate code that uses shock-fitting to compute the location of the bow shock on a straight blunt cone. This base geometry and high-order shock-fitting approach has been validated extensively for accuracy.[14]

A. Governing Equations

The DNS code solves the conservation-law form of the three-dimensional Navier-Stokes equations in Cartesian coordinates. Written in vector form, the governing equations are

$$\frac{\partial U}{\partial t} + \frac{\partial F_j}{\partial x_j} + \frac{\partial G_j}{\partial x_j} = 0, \tag{2}$$

in which U is the state vector of conserved quantities, F_j is the inviscid flux vectors, and G_j is the viscous flux vector in the j^{th} spatial direction. The state and flux vectors are defined as,

$$U = \{\rho,\ \rho u_1,\ \rho u_2,\ \rho u_3,\ e\}^T, \tag{3}$$

$$F_j = \{\rho u_j,\ \rho u_1 u_j + p\delta_{1j},\ \rho u_2 u_j + p\delta_{2j},\ \rho u_3 u_j + p\delta_{3j},\ (e+p)u_j\}^T, \tag{4}$$

and

$$G_j = \{0,\ \tau_{1j},\ \tau_{2j},\ \tau_{3j},\ \tau_{jk}u_k - q_j\}^T, \tag{5}$$

where e is internal energy, τ_{ij} is viscous stress tensor, and q_j is the heat flux. The internal energy, viscous stress, and heat flux, q_j, are defined as follows,

$$e = \rho\left(c_v T + \frac{u_k u_k}{2}\right), \tag{6}$$

$$\tau_{ij} = \mu\left(\frac{\partial u_i}{\partial x_j} + \frac{\partial u_j}{\partial x_i}\right) + \delta_{ij}\lambda\frac{\partial u_k}{\partial x_k}, \tag{7}$$

and

$$q_j = -\kappa\frac{\partial T}{\partial x_j}. \tag{8}$$

Equation 2 is closed assuming a calorically perfect gas,

$$p = \rho R T. \tag{9}$$

Which is a fair assumption for low-enthalpy hypersonic flows. The properties of nitrogen gas are used, which is consistent with the experimental case from which this simulation takes its parameters.[15] The specific heats c_p and c_v are held constant with a given specific heats ratio of $\gamma = 1.4$. A specific gas constant of $R = 296.8 J/kgK$ for nitrogen gas is used. The viscosity coefficient, μ, is calculated by Sutherland's law in the form:

$$\mu = \mu_r\left(\frac{T}{T_o}\right)^{3/2}\frac{T_o + T_s}{T + T_s} \tag{10}$$

where $\mu_r = 1.7894 \times 10^{-5}$ N·s/m^2, $T_o = 288.0$ K, and $T_s = 110.33$ K. Lastly, the Prandtl number is taken as $-2/3\mu$ and the thermal conductivity, κ, is computed from the constant Prandtl number,

$$\kappa = \frac{c_p \mu}{Pr}. \tag{11}$$

Fong and Zhong,[16] Huang and Zhong,[17] and Lei and Zhong[18] have used the same formulation or similar formulations for simulating perfect gas hypersonic flow.

B. Numerical Methods

A shock-fitting method is used to obtain a defined shock location. The shock-fitting method treats the shock as the upper boundary of the physical domain by computing the location of the bow shock produced by the blunt cone. Eq. (2) is solved in a computational domain with body-fitted curvilinear coordinates (ξ, η, ζ, τ), where ξ is in the direction of the cone surface, η is normal to the cone surface, ζ is in the azimuthal direction, and τ is time. Treating the shock as a domain boundary, the transient shock movement is solved as an ODE alongside the governing equation. The transformation relations between the physical domain and computational domain are

$$\begin{cases} \xi = \xi(x,y,z) \\ \eta = \eta(x,y,z,t) \\ \zeta = \zeta(x,y,z) \\ \tau = t \end{cases} \Leftrightarrow \begin{cases} x = x(\xi,\eta,\zeta,\tau) \\ y = y(\xi,\eta,\zeta,\tau) \\ z = z(\xi,\eta,\zeta,\tau) \\ t = \tau \end{cases}. \tag{12}$$

Applying this transformation to Eq. (2) obtains the governing equations in computational space,

$$\frac{1}{J}\frac{\partial U}{\partial \tau} + \frac{\partial E'}{\partial \xi} + \frac{\partial F'}{\partial \eta} + \frac{\partial G'}{\partial \zeta} + \frac{\partial E'_v}{\partial \xi} + \frac{\partial F'_v}{\partial \eta} + \frac{\partial G'_v}{\partial \zeta} + U\frac{\partial (1/J)}{\partial \tau} = 0, \tag{13}$$

where J is the Jacobian of the coordinate transformation and

$$\begin{aligned} E' &= \frac{F_1\xi_x + F_2\xi_y + F_3\xi_z}{J}, F' = \frac{F_1\eta_x + F_2\eta_y + F_3\eta_z}{J}, G' = \frac{F_1\zeta_x + F_2\zeta_y + F_3\zeta_z}{J}, \\ E'_v &= \frac{G_1\xi_x + G_2\xi_y + G_3\xi_z}{J}, F'_v = \frac{G_1\eta_x + G_2\eta_y + G_3\eta_z}{J}, G'_v = \frac{G_1\zeta_x + G_2\zeta_y + G_3\zeta_z}{J}. \end{aligned} \tag{14}$$

Full transformation details can be found in Zhong 1998.[14]

The shock position and velocity must be obtained of the form $H(\xi, \zeta, \tau)$ and $H_\tau(\xi, \zeta, \tau)$ and solved as independent flow variables alongside the governing equations. This is accomplished by taking the Rankine-Hugoniot relations, which provide the flow variable boundary conditions behind the shock, as a function of U_∞ and the velocity of the shock front v_n. The shock front velocity is determined by a characteristic compatibility equation at the grid point immediately behind the shock. A complete derivation of H and H_τ can also be found in Zhong, 1998.[14]

An explicit 5^{th}-order upwind scheme and an explicit 6^{th}-order central finite-difference scheme are used to discretize the inviscid and viscous terms of Eq. 13 in the ξ and ζ-directions. A seven point stencil is used in both instances;

$$\frac{\partial f_i}{\partial x} = \frac{1}{hb_i}\sum_{k=-3}^{3}\alpha_{i+k}f_{i+k} - \frac{\alpha h^5}{6! b_i}\frac{\partial f^6}{\partial^6 x}, \tag{15}$$

where

$$\alpha_i = -\frac{5}{3}\alpha, \quad \alpha_{i\pm1} = \pm 45 + \frac{5}{4}\alpha, \quad \alpha_{i\pm2} = \mp 9 - \frac{1}{2}\alpha, \quad \alpha_{i\pm3} = \pm 1 + \frac{1}{12}\alpha, \quad b_i = 60, \tag{16}$$

and h is the step size. An $\alpha = -6$ is used to achieve a low dissipation upwind scheme for the inviscid terms, and $\alpha = 0$ is used to yields a central scheme for the viscous terms. Second order derivatives are obtained by applying Eq. (15) twice. Derivatives in the η-direction are computed using Fourier collocation since the case is axisymmetric. Flux spitting is use on the inviscid flux terms resulting in

$$F' = F'^{+} + F'^{-} \quad \text{where} \quad F'^{\pm} = \frac{1}{2}(F' \pm \Lambda U), \tag{17}$$

and Λ is a diagonal matrix that ensures F'^{+} and F'^{-} contain only pure positive and negative eigenvalues respectively. A low storage 3rd-order Runge-Kutta method[19] is used to converge the steady state and advance the unsteady solutions.

C. Direct Numerical Simulation of Disturbances

To simulate unsteady disturbances, a blowing-suction actuator is used to introduce a pulse into a converged steady state. The actuator extends circumferentially around the cone. The pulse has a Gaussian shape

in time and is sinusoidal in space. The sinusoidal shape prevents introducing additional mass into the mean flow. The frequency spectrum of the pulse is chosen to be broad enough as to include the most unstable mode frequencies for the given flow conditions. Downstream of the actuator, each frequency is examined for amplification or dampening. This technique of using a Gaussian pulse to examine mode amplification/dampening was previously implemented by Fong and Zhong[20] and Knisely and Zhong.[3,4]

The actuator mass flux follows the equation,

$$\dot{m}_p(s,t) = \varepsilon(\rho U)_\infty \exp\left(-\frac{(t-\mu)^2}{2\sigma^2}\right)\sin\left(2\pi\frac{s-s_c}{l}\right) \tag{18}$$

for $s_c < s < s_c + l$ and $t > 0$. In which μ is the mean, σ is the standard deviation, s_c is the starting location for the actuator along the surface, and l is the length of the actuator. The mass flux is scaled by $\varepsilon(\rho U)_\infty$. The mean of the pulse is defined in terms of a mass flux minimum, $(\rho v)_{min}$, which is the initial mass flux at t=0. Naturally, $(\rho v)_{min}$ is very small, preferably close to zero, however not too small that an appreciable amount of computational time has to pass before the pulse fully develops. The equation for μ is given as,

$$\mu = \sqrt{-2\sigma^2 ln\left(\frac{(\rho v)_{min}}{\varepsilon(\rho U)_\infty}\right)}. \tag{19}$$

By defining μ in this way, μ can be fixed with a reasonable $(\rho v)_{min}$ regardless of the simulation conditions. Thus, by design, the only remaining free parameter in Eq. (18) is σ which permits direct control over the frequency content of the pulse. Hence, when setting the pulse for a particular case, only the standard deviation needs to be modified. The pulse parameters used in this paper are given in Table 1, moreover the time history of Eq. (18) and its corresponding FFT are given in Fig. 1.

Table 1: Pulse parameters

Parameter	ε	$(\rho v)_{min}$ [kg m/s]	σ [μs]	μ [μs]	x_s [m]	l [mm]
Value	10^{-3}	10^{-10}	0.3	2.0398	0.1976	1.9703

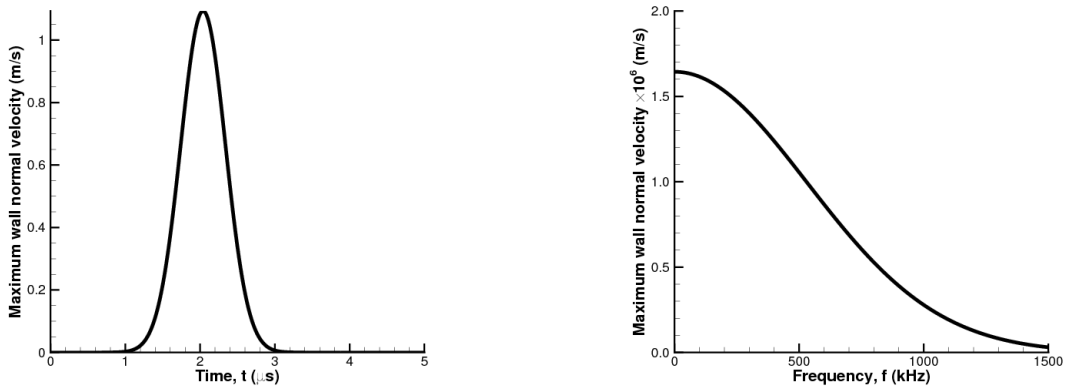

(a) (b)

Figure 1: (a) Time history of the maximum wall normal velocity. (b) FFT of maximum wall normal velocity in (a).

III. Freestream and Simulation Conditions

The simulation is based on a slender straight blunt cone geometry at zero angle-of-attack. The cone has a 7° half-angle and a nose radius of 0.5 mm with a total length of 1.0 m measured from the blunt nose tip.

The simulation is axisymmetric. The freestream conditions are taken from a previous experiment performed in SNL Hypersonic Wind Tunnel for the same cone geometry.[15] The freestream conditions are listed in Table 2.

Table 2: Simulation Parameters

Parameter	Value	Unit
M_∞	8.0	-
ρ_∞	0.024803	kg/m^3
p_∞	330.743	Pa
T_∞	44.9	K
T_o	620.0	K
T_w	279.0	K
γ	1.4	-
Pr	0.72	-
Re_∞/l	9584257	m^{-1}

Figure 2a contains the steady state pressure and temperature results for the frustum of the cone. Overall the results are typical of a straight blunt cone. The pressure results on the top half of the cone show a moderate pressure ratio, relative to the freestream pressure, along the majority of the cone. The steady state was deemed converged once the pressure error reached $O(\epsilon_p) = 10^{-9}$.

In the bottom half of fig. 2a, the temperature ratio is also typical of a straight blunt cone. The contours show a high thermal gradient between the boundary-layer and the flow behind the shock, which extends over the majority of the frustum. This is to be expected as the simulation assumes a constant wall temperature, which is considerably higher than the freestream temperature.

Taking a closer look at just the blunt nose tip of the cone in fig. 2b, the steady state pressure and temperatures results are presented together. The pressure contours show a maximum pressure ratio at the very tip of the cone followed by a favorable pressure gradient moving downstream. It is also apparent that the moderate pressure ratios seen on the frustum are reached within approximately eight nose radii of the tip. The temperature contours too show a maximum temperature ratio at the cone tip. The maximum however is just offset from the cone surface. This is due to the constant wall temperature boundary condition, which does not consider surface heating. Moving downstream, the temperature ratios seen along the cone frustum are also reached within eight nose radii.

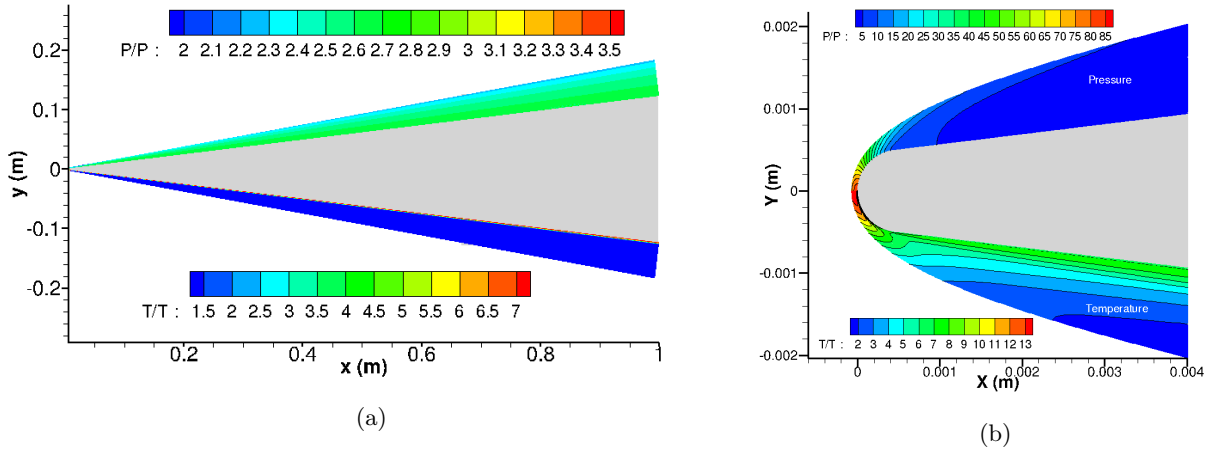

(a) (b)

Figure 2: Pressure & temperature contours on the (a) cone frustum at the (b) blunt nose tip. The figures are split with pressure plotted on the top half and temperature plotted on the bottom half.

IV. Results

Much of the linear stability analysis of the steady state has been carried out in Haley et al.[1] and shall not be repeated presently. Instead this paper will focus on the new supersonic mode wave structures seen in the unsteady results.

A. Unsteady results on a smooth cone

Figure 3 shows the propagation of the disturbance downstream as it develops features of the supersonic mode. The blowing-suction actuator is located at $s_c = 0.2m$. The contour levels are clipped so that the pressure perturbations in the shock layer are more visible. In general the maximum $|\Delta p|$ is on the order of 10^0. Figure 3a shows the traveling pulse; its appearance is consistent with an unstable second mode. As the pulse moves further downstream, fig. 3b shows a slight "pulling-apart" of the pulse which would indicate that the mode families within the pulse are traveling at two different group velocities. fig 3c shows the acoustic-like waves emanating from the boundary layer which is considered indicative of the supersonic mode.

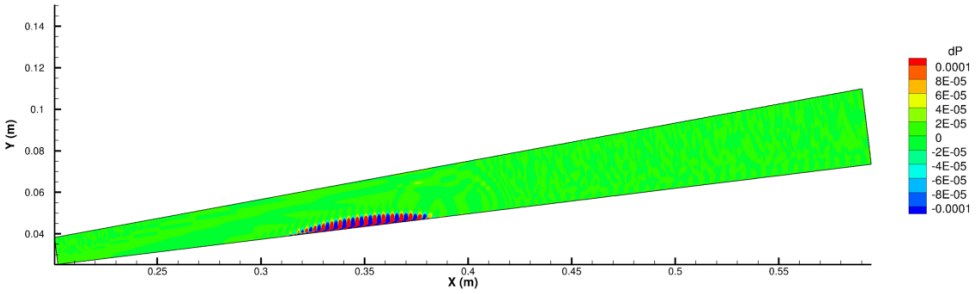

(a)

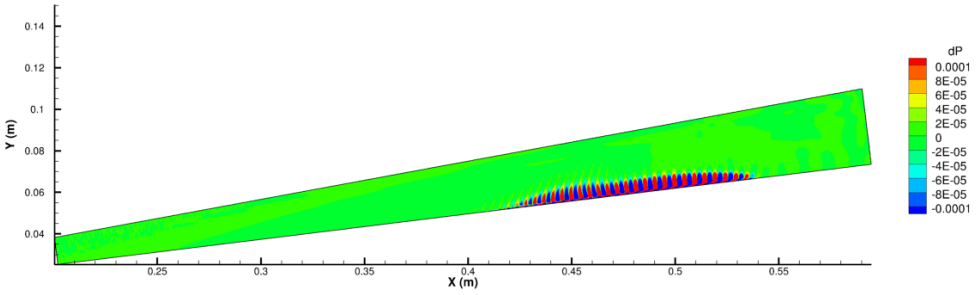

(b)

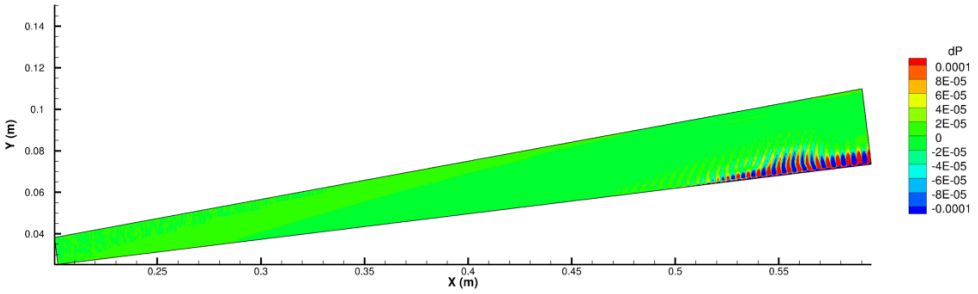

(c)

Figure 3: (a) The pulse excites Mack's 2nd mode instability. (b) As the pules propagates downstream, it develops a primary and satellite wave. (c) Acoustic-like waves propagate into the shock layer from in between the primary and satellite waves.

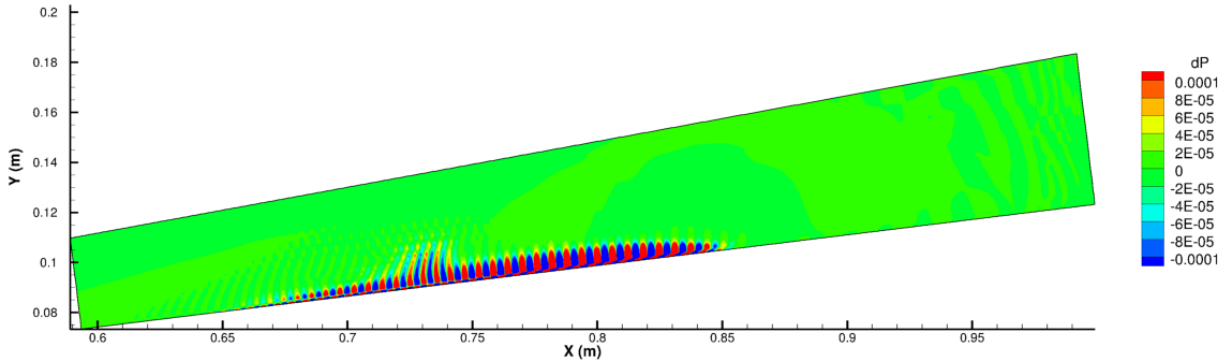

(a)

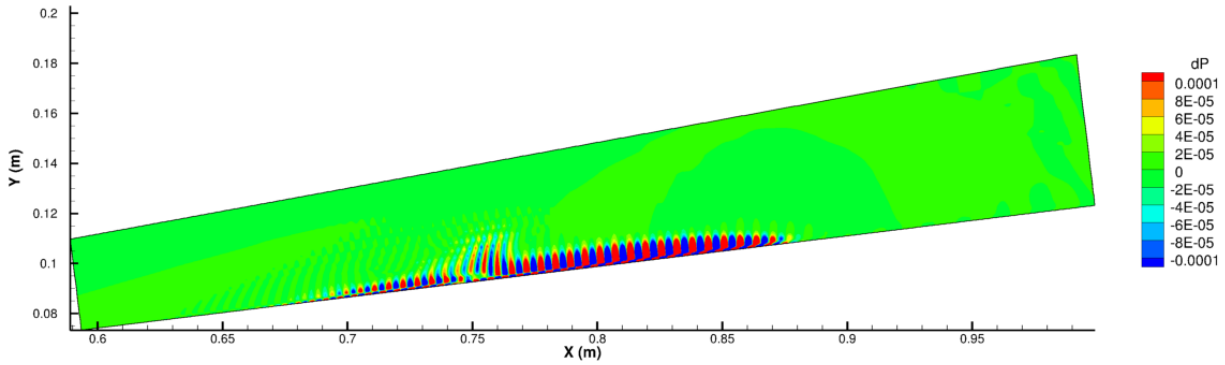

(b)

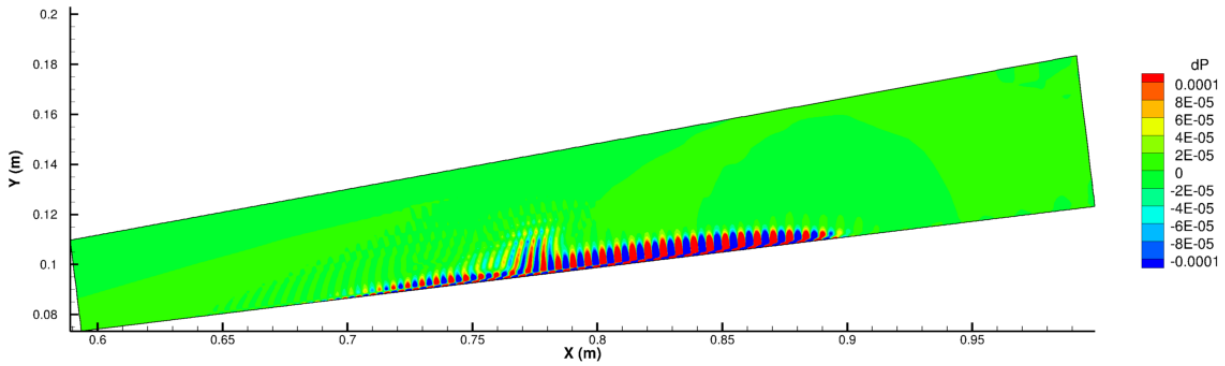

(c)

Figure 4: (a) The acoustic-like waves seen in context of the entire wave packet. (b) A dead zone develops in the boundary layer due the destructive interference of the wave groups. (c) The dead zone is relatively stationary to the pulse and eventually disappears.

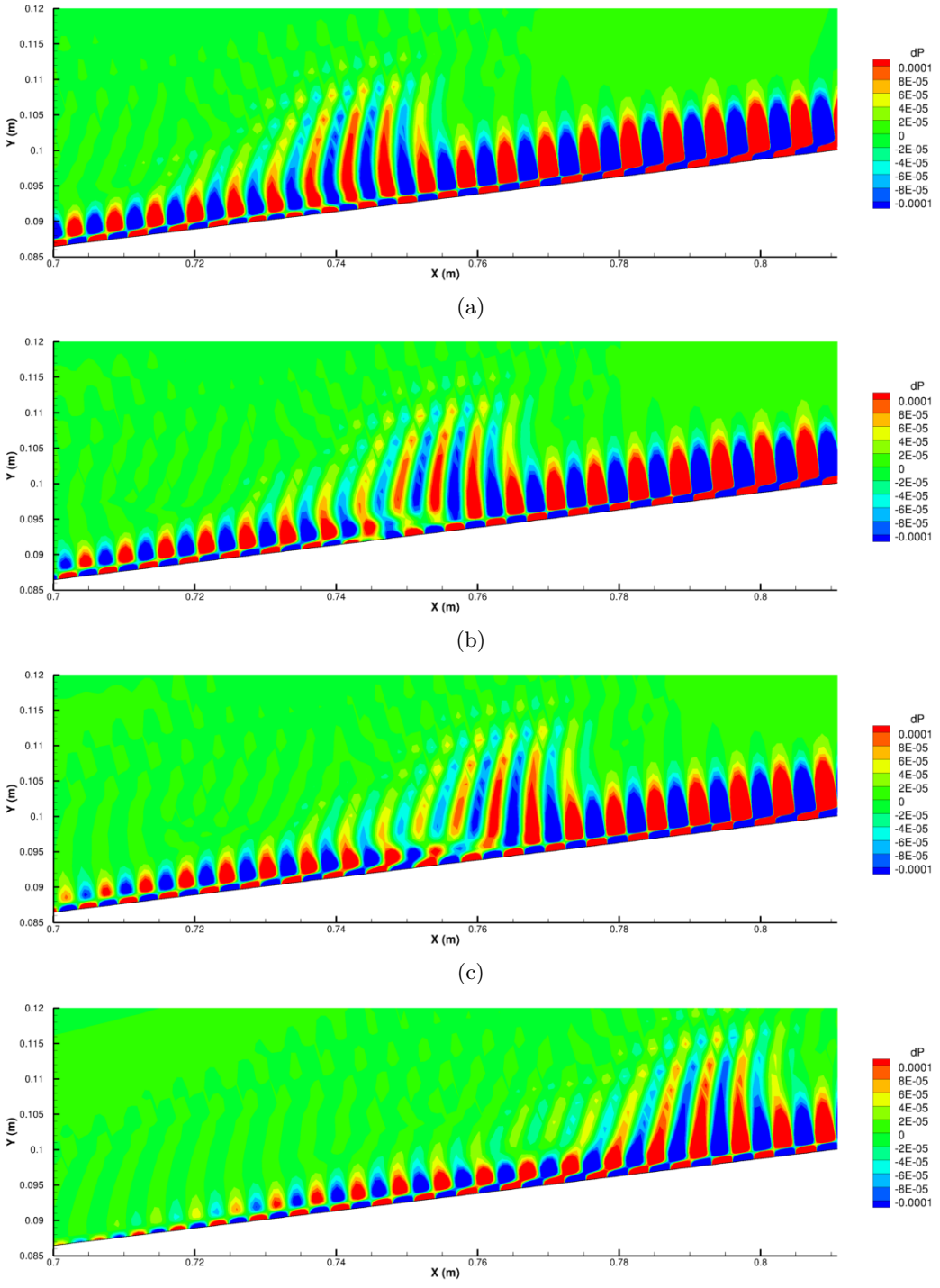

Figure 5: Progression of pulse interference patterns.

Figure 4 shows the same pulse as it propagates even further downstream. Here we see that the pulse has grown in width due to dispersion and the acoustic-like waves are more apparent. These acoustic-like waves demark the upstream portion, or primary wave, and the downstream portion, or satellite waves. LST results presented later will show that the primary wave is mode S dominant and the satellite waves are mode F dominant. Since the primary and satellite waves are dispersive in nature their widths grow. This means the two parts of the pulse are capable of interfering with one another; this is what we see in fig. 4b as evidenced

by a dead zone in the wave train. The dead zone originates on the surface due to destructive interference between the primary and secondary satellite waves. The dead zone is also relatively motionless in the lab frame and eventually exits the disturbance all together as it propagates downstream as seen in fig. 4c.

Figure 5 provides a more detailed look at the interference phenomenon. Figure 5a shows the pulse before the interference takes place. In fig. 5b, oscillations below the sonic line centered about $x = 0.745m$ weaken in strength as they start to cancel. Above the sonic line and the oscillations around $x = 0.75 - 0.755m$ begin to interfere creating the dead zone. By fig. 5c the weakening oscillations below the sonic line have canceled out completely and the dead zone appears to move upstream relative to the pulse. By fig. 5d, the pulse assumes the same appearance as in fig. 5a before the wave interference began. Along the $1m$ length of the cone ($0.782m$ if we deduct the length of upstream of the blowing suction slot) the interference pattern appears six times. All throughout this process acoustic-like waves are emanating from the wave train.

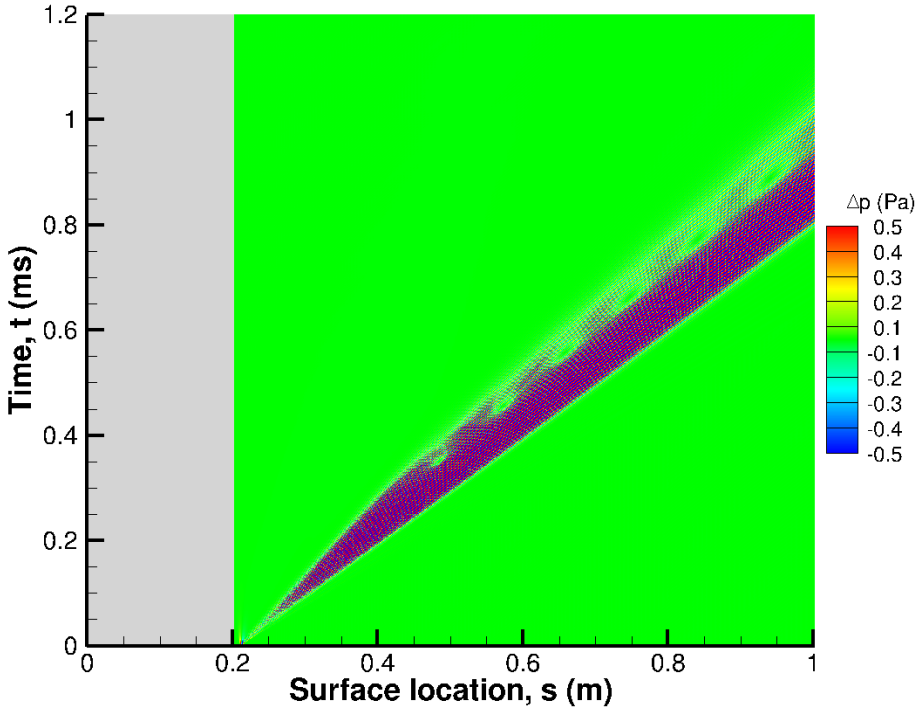

Figure 6: x-t diagram of unsteady pulse for actuator located $s_c = 0.2m$. Contours are clipped to show weaker satellite wave; $\max|\Delta p = 9.635(Pa)|$.

One way to view the propagation of the disturbance is to plot in an x-t diagram. Figure 6 plots the pressure perturbation along the surface of the cone for the entirety of the unsteady simulation; the area upstream of the actuator at $s_c = 0.2m$ is grayed out. The maximum and minimum contour levels are clipped to highlight the satellite wave. As expected the disturbance fans out downstream as the boundary layer is inherently dispersive and different frequencies propagate at different speeds. The wavefront propagates with a speed of $980m/s$ ($c_r \approx 0.897$ based on U_∞) with following waves propagating at slower speeds. The x-t diagram exhibits six patches of destructive wave packet interference. The patches occur at nearly regular intervals increasing slightly downstream. The interference patches also increase in size and duration downstream. The speed of the patches, measured from first to last is 847.14 m/s ($c_r \approx 0.775$ based on U_∞). This speed is a slight cheat because the interference patches do not follow a ray originating from the actuator at $t = 0$ and $s_c = 0.2m$, but it should illustrate that the satellite wave packet to the left of it is propagating at supersonic phase speeds ($c_r < 1 - 1/M_\infty$).

One last feature to note in fig. 6 is the speed of the wave train tail; between $0.20m$ and $0.42m$ the tail is steeper and therefore slower, afterwards the tail is shallower indicating a speed up. Temporally this corresponds to when the primary and satellite wave packet first appears and starts undergoing construc-

tive/destructive interference (see fig. 6 at $t = 0.312ms$). Spatially this corresponds with the disturbance's maximum pressure perturbation, which occurs earlier in time.

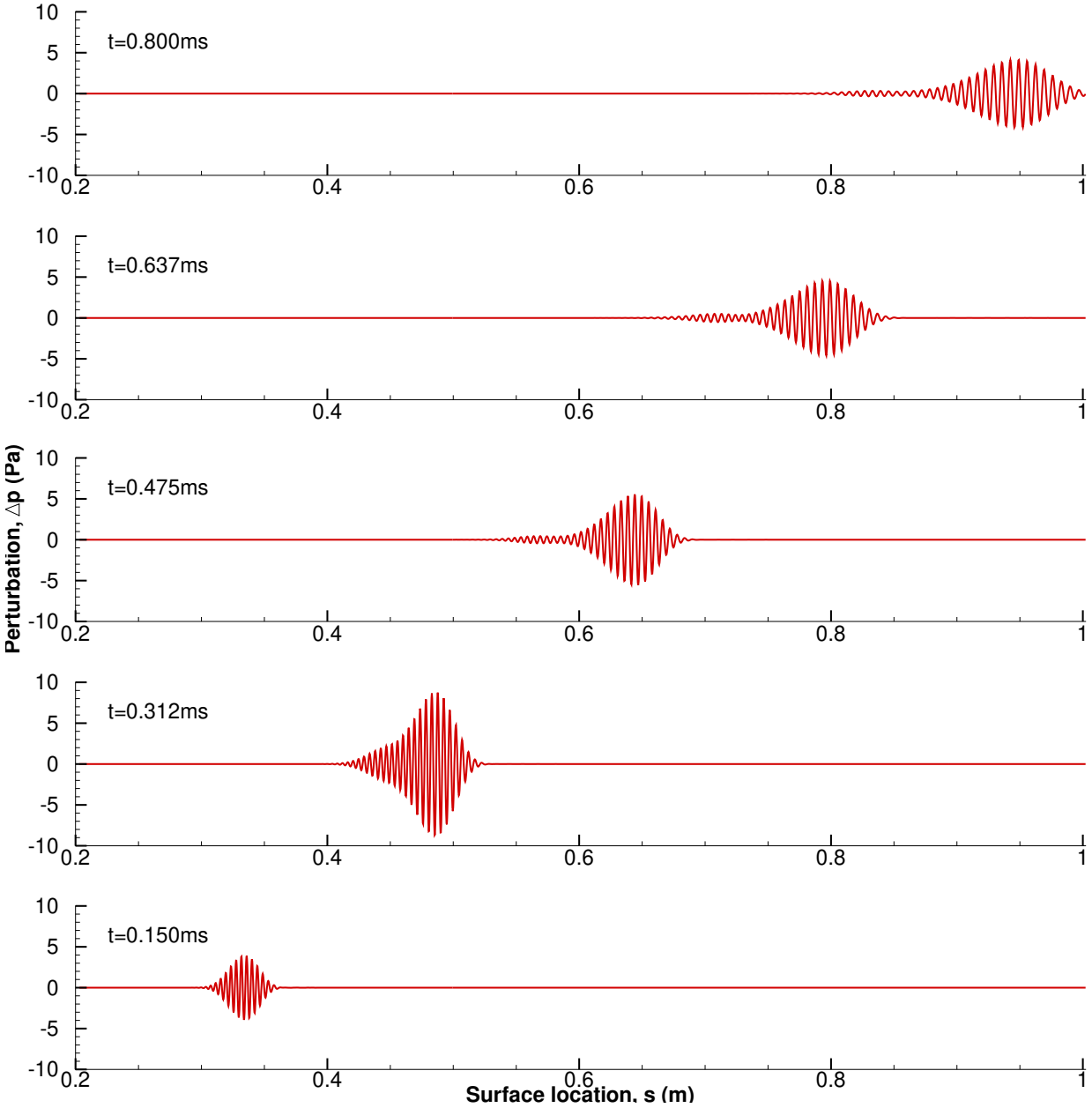

Figure 7: Propagation of disturbance from actuator located $s_c = 0.2m$.

Although the x-t diagram provides and entire overview of the unsteady disturbance. It is difficult to discern the structure of the disturbance. Figure 7 features time traces along the surface taken at regular intervals of $0.163ms$. At $t = 0.150ms$ the disturbance appears as a single wave packet; this is typical of previous unsteady simulations[3,4] after the initial forcing by the actuator. Between $t = 0.150ms$ and $t = 0.312ms$ the disturbance grows, nearly doubling in strength. This is the expected behavior as the boundary layer is unstable, however, by $t = 0.312ms$ we already see the emergence of a satellite wave packet. By $t = 0.475ms$ the satellite wave packet is full formed; it is considerably weaker, $max|\Delta p| = 0.44Pa$ compared to the primary waves at $5.49Pa$. Of particular note is that between $t = 0.312ms$ and $0.475ms$ the primary wave weakens and remains weaker for the remainder of the simulation. This is unexpected behavior, typically disturbances are expected to grow downstream in unstable hypersonic boundary layers.

For the intervals between $t = 0.475ms$ and $0.800ms$ the satellite wave packet is clearly present and similar in strength. Lastly, the intervals in fig. 7 show that the wave train as a whole has lengthened due to dispersion.

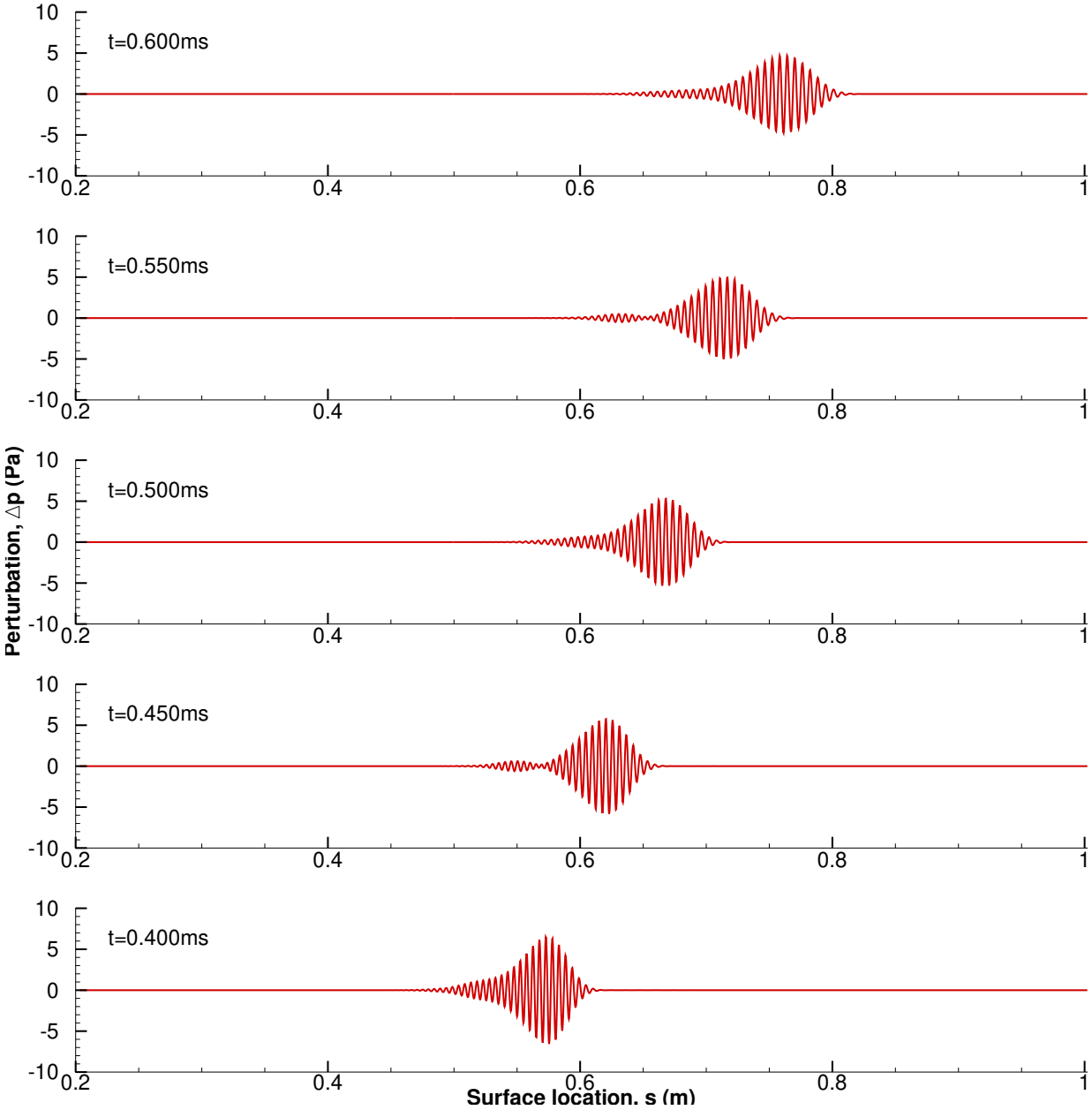

Figure 8: Interference of primary and satellite waves. Actuator located $s_c = 0.2m$.

Figure 8 takes a closer look at the interference between the primary and satellite waves. The interval from $t = 0.400ms$ and $0.600ms$ includes the second and third patches seen in fig. 7. At $t = 0.400$, 0.500, and $0.600ms$, the satellite wave packet appears as a tail of the primary wave packet. It is conjectured that constructive interference between the wave packets gives rise to the acoustic-like waves radiating into the boundary layer as seen in figs. 3 and 4. Since the primary and satellite waves are dispersive, occasionally the waves will interfere destructively, these are the patches seen in fig. 6 and the dead zones seen in fig. 5.

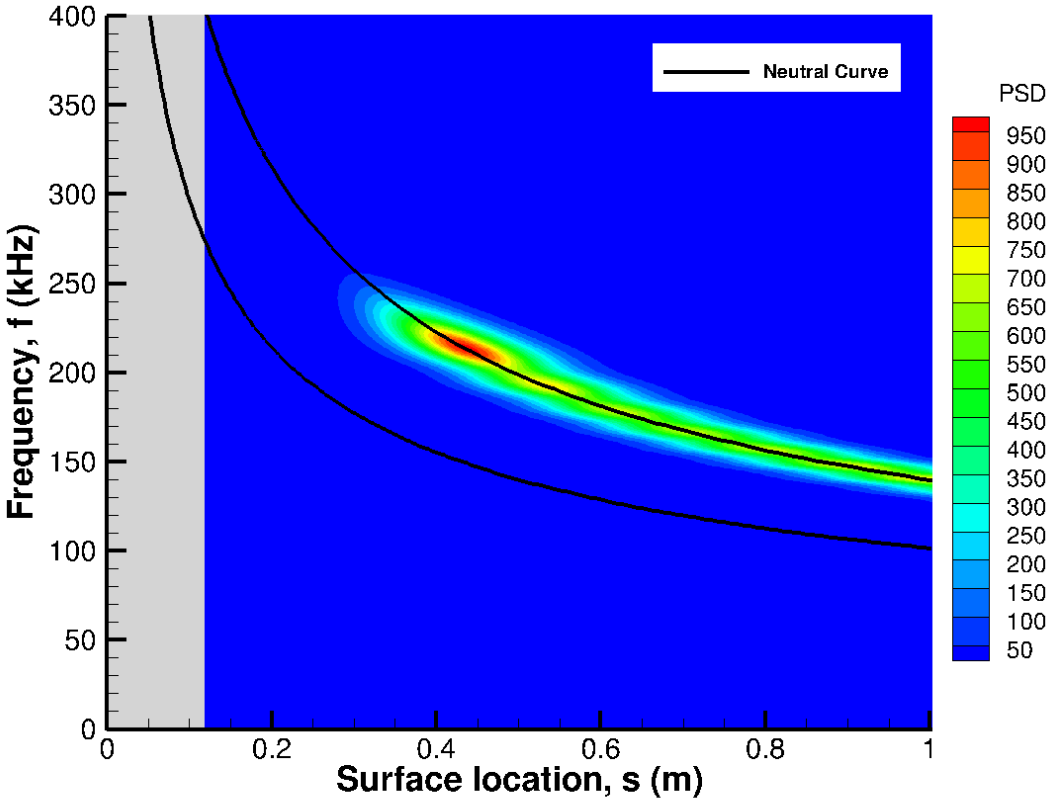

Figure 9: PSD of disturbance from actuator located s=0.2m.

To see which frequencies undergo constructive and destructive interference, an FFT analysis on the temporal data in fig. 6 can extract the spectral data. The power spectrum density (PSD) is featured in fig. 9. The spectrum is normalized by the PSD of the blowing-suction actuator in order to evaluate the growth and decay of each frequency irrespective on its initial strength. The neutral curve for mode S, obtained from LST analysis, is plotted on top of the PSD contour. There is really good agreement between the FFT and LST; as expected the PSD of each frequency visibly grows to the left of the branch II neutral curve and dampens to the right. Since growth rates are unstable between branch I and branch II, and stable everywhere else, the PSD is expected to grow and decay.

As previously mentioned, the time traces are atypical since the disturbance did not grow steadily downstream, but instead shows the greatest growth around $s = 0.438m$. The reason for this is unclear but its occurrence and the occurrence of the interference patterns are probably not independent. From the FFT, the maximum PSD corresponds to a frequency of $213.67kHz$. It is thought that the atypical growth is a result of receptivity at the actuator location. The center of the actuator is located at $s_c = 0.2m$ which is close to the maximum PSD frequency's branch I neutral point. Making the boundary highly susceptible to disturbances with this frequency. That said, the initial pulse is appropriately small in order to maintain linearity, as such the PSD grows nearly three orders of magnitude. If the primary focus on this paper were on transition, it is likely that a stronger initial pulse would have led to transition (it is worth noting that the experiment this simulation borrows its conditions from see intermittent turbulence start around $0.30m$,[15] however that test article does not extend beyond $0.5m$).

The FFT also exhibits the constructive/destructive interference and the frequencies they are centered around for each. The destructive interference occurs around 200kHz, 184 kHz, 171kHz, 161kHz, 152kHz, and 143kHz, with the constructive interference occurring around 192kHz, 178kHz, 166kHz, 156kHz, 147kHz, and 139kHz. Note that the differences between successive frequencies becomes smaller with decreasing frequency.

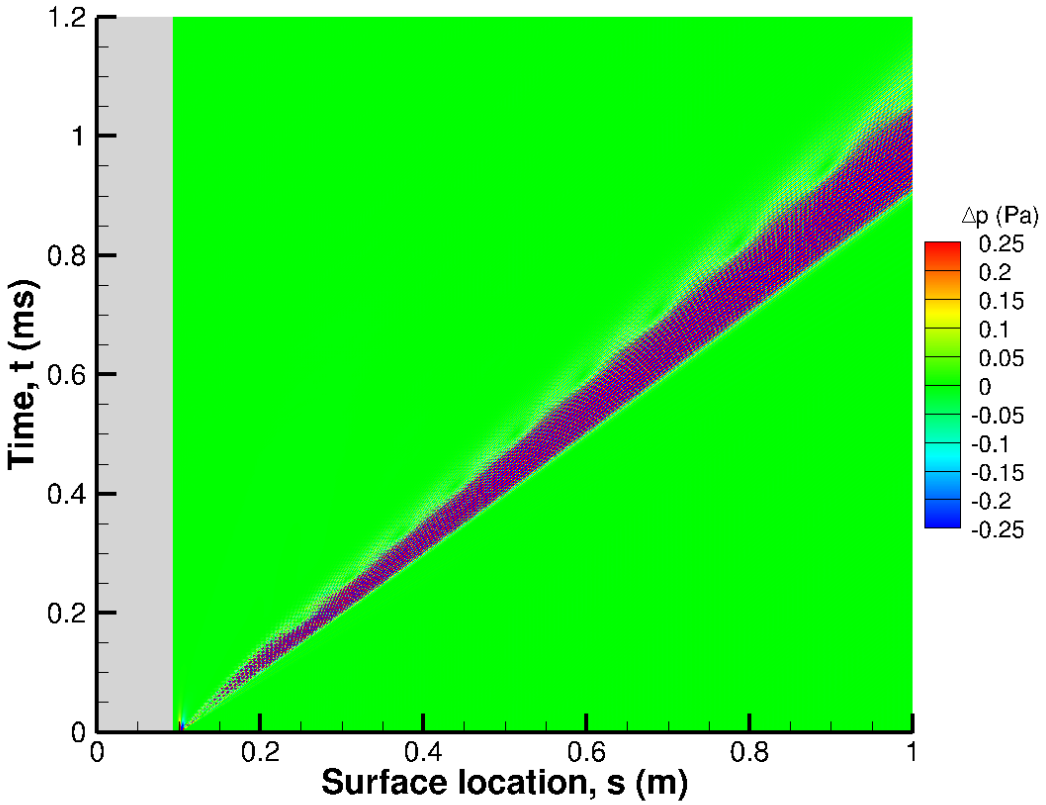

Figure 10: x-t diagram of unsteady pulse for actuator located s=0.1m. Contours are clipped to show weaker satellite wave; $\max|\Delta p = 3.098(Pa)|$.

A second unsteady simulation was carried out with the blowing-suction actuator closer upstream centered about $s_c = 0.10m$. The x-t diagram in fig. 10, like the previous x-t diagram, features the complete unsteady disturbance along the cones surface. The result is more typical of unsteady surface pulses, where the wave is more tightly confined, with the wave front traveling at $\approx 983.6m/s$ ($c_r = 0.900$ based on U_∞) and the tail traveling at $\approx 798.6m/s$ ($c_r = 0.731$ based on U_∞). As such, dispersion has caused the wave to lengthen downstream. Figure 10 also contains the conspicuous interference patches seen with the downstream actuator. These are also the result of destructive interference between primary and satellite waves, however, this time the satellite wave is almost non-existent, forming an almost sawtooth-like pattern with the interference patches. The less prominent satellite wave is thought to be due to a weaker receptivity response from the actuators location.

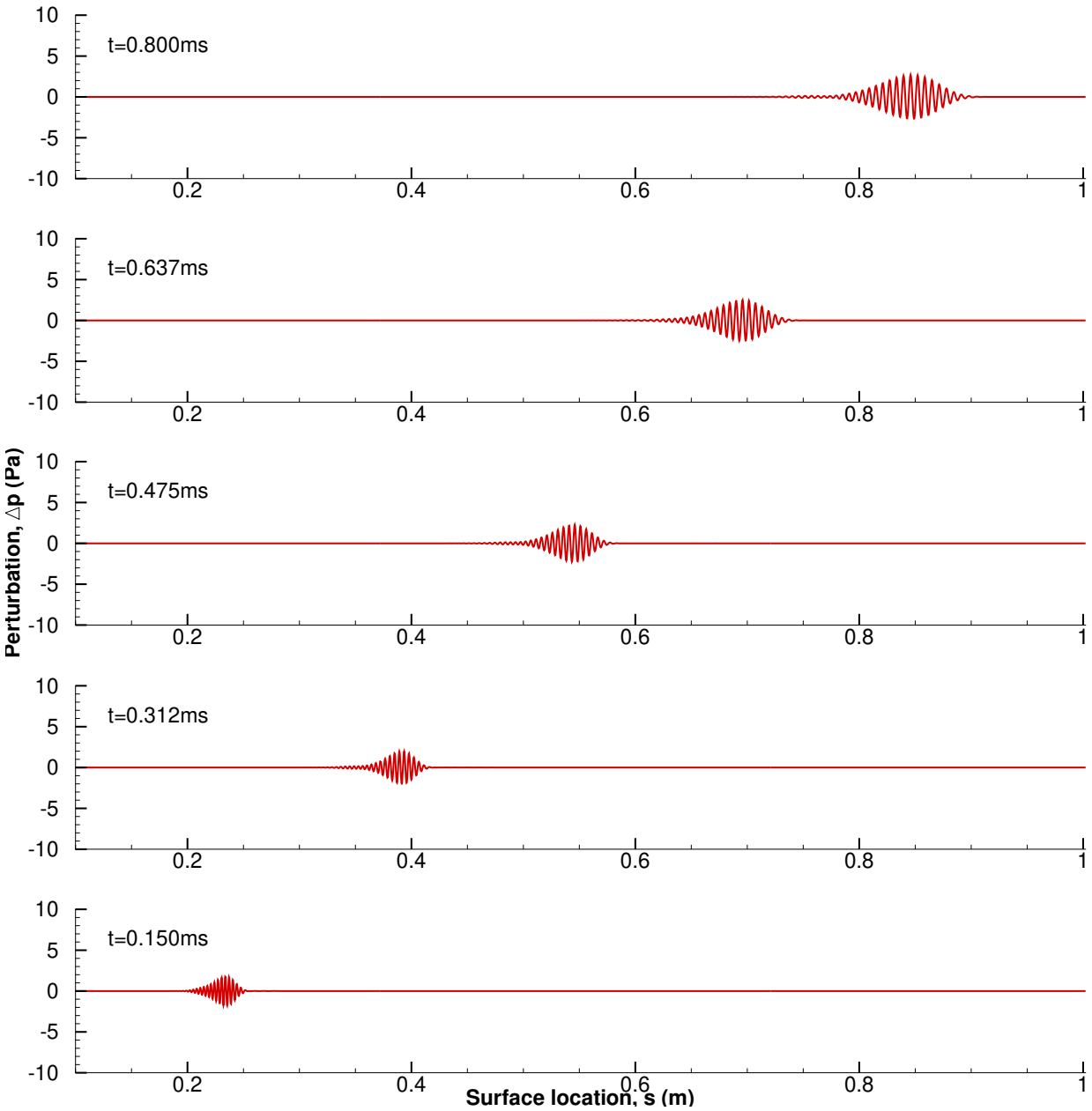

Figure 11: Propagation of disturbance from actuator located s=0.1m.

Examination of individual time traces, like those in fig. 11 reveals that the structure of the disturbance is more typical for unsteady surface pulses. As expected the unsteady boundary layer causes the disturbance to grow downstream. From $t = 0.150$ to $0.800ms$ the maximum perturbation grows from $1.738Pa$ to $2.707Pa$, a 59% increase. The growth is very mild compared to the downstream actuator case, which although having the same actuator strength, saw a larger disturbance perturbation. The satellite wave is also present as a tail on the primary wave, and is even less prominent that the satellite wave in fig 11.

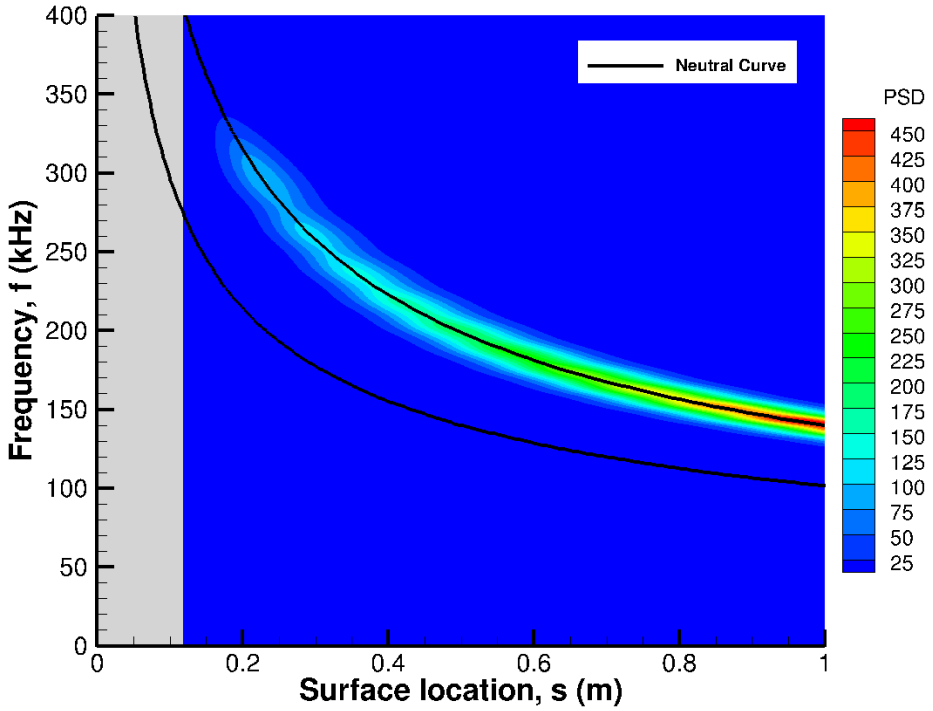

Figure 12: PSD of disturbance from actuator located s=0.1m.

As before, an FFT of the temporal data is used to obtain the spectral analysis. Figure 12 contains both the spectrum and neutral curve for the upstream actuator. Like before the PSD agrees well with the neutral curve. Overall the PSD increases downstream with decreasing frequency. The initial wobbliness in the contours is most likely due to the forcing by the actuator. Again the location of the actuator places it at the branch I neutral point for 292kHz, unlike the downstream actuator there is no strong receptivity response. Farther downstream there is a slight meandering of the PSD contours, this appears to be a result of the constructive/destructive interference seen in fig. 10, however since the satellite wave is much weaker the same local maxima and minima do not appear in the spectrum as they do in fig. 12.

B. LST analysis of steady state.

The unsteady results provide an excellent description of how a disturbance evolves over time in an unsteady boundary layer. But to understand the boundary layer's stability we must look to linear stability theory (LST). LST is applied to the steady state solution of the simulation in order to obtain the discrete boundary layer modes: mode F and mode S. For this particular spatial analysis a frequency of 160kHz is selected because it coincides with a downstream interference patch (the fourth patch in particular) as seen in fig. 6. The location is downstream of the peak PSD but also not at the end of the cone. Figure 13a contains the phase speeds of Mode F and S. Mode F originates in the fast acoustic spectrum ($c_r = 1 + 1/M_\infty$) by definition and steadily slows down until it passes through the continuous spectrum ($c_r = 1$) and slow acoustic spectrum ($c_r = 1 - 1/M_\infty$). The break in the curve is because the LST code had difficulty resolving the mode near the continuous spectrum branch cut and near the Mode F/S coupling. Of particular interest to the paper however is when mode F becomes supersonic at $c_r < 1 - 1/M_\infty$ after $s = 0.605m$. The phase velocity calculated from the x-t diagrams in figs. 6 and 10 indicate that the satellite wave phase velocity falls in this range.

This means that the satellite wave is comprised of mode F. When the phase velocity of any discrete mode is supersonic it creates as situation in which acoustic-like waves can emit into the shock layer. A glance

at fig. 13b, which contains the modal growth rate, however, shows that mode F is stable. Therefore any acoustic-like waves are unlikely to be sustained; for that we must look at mode S.

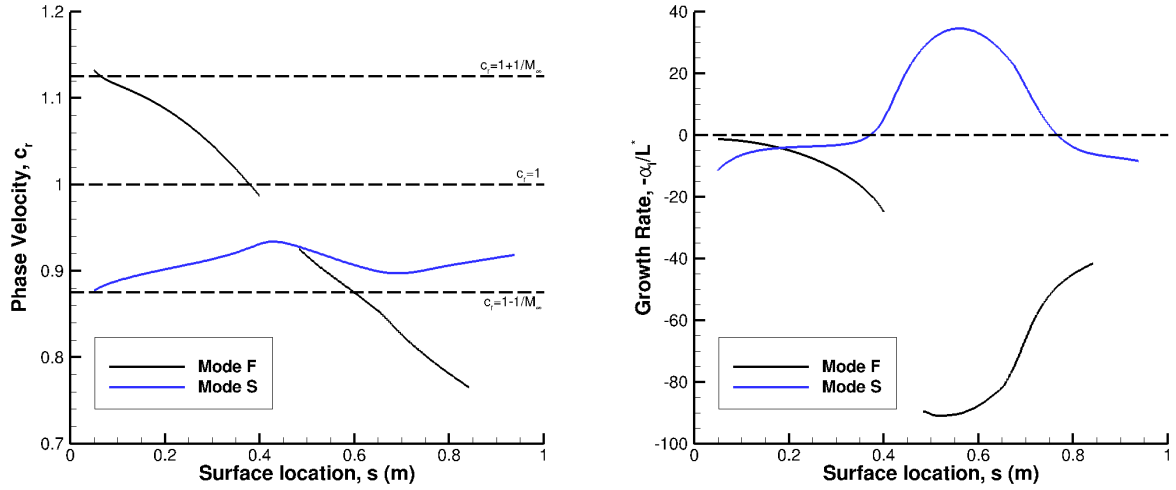

(a) (b)

Figure 13: (a) Phase velocity and (b) growth rate at $f = 160kHz$

Unlike mode F, the LST code had no difficulty resolving the curve. Figure 13a shows that mode S originates from the slow acoustic spectrum, as it should and takes on a phase velocity between $c_r = 1$ and $c_r = 1 - 1/M_\infty$. These phase velocities are consistent with the phase velocities of the primary wave in figs. 6 and 10 indicating that the primary wave is comprised of mode S. Looking now to the growth rate in fig. 13b, mode S starts stable and clearly becomes unstable due mode F/S coupling, this is Mack's second mode instability (the first mode is stable). It is because of this instability that the disturbance in fig. 7 was expected to grow downstream. Moreover the N-factor, computed from LST results, also expected any disturbances to grow downstream; as seen in fig. 14 the boundary layer becomes increasing unstable. The reality is that the disturbance in fig. 7 does not grow downstream because of strong constructive/destructive interference between mode S and mode F.

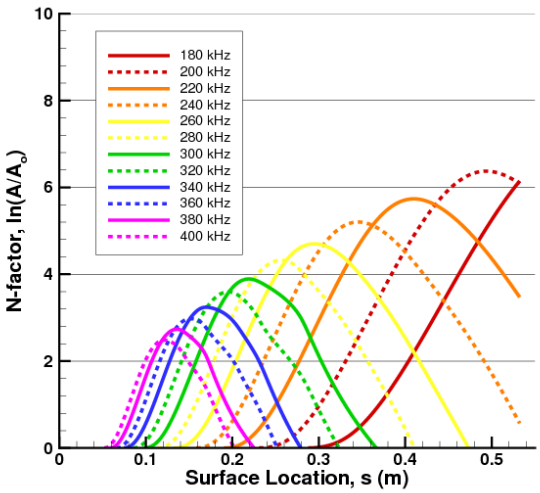

Figure 14: N-factor obtained from LST.

V. Conclusion

This supersonic mode result was found unexpectedly while studying the transition-delaying roughness effect. The low-enthalpy and warm wall simulation parameters are far removed from the high-enthalpy, cold wall parameters in which acoustic-like waves emanating from the boundary layer are typically seen. The acoustic-like waves seen in this paper, however, emerge very differently than those seen in other studies. Those supersonic modes are typically the result of a discrete mode (either mode F or S) that is both unstable and propagating with a phase speed less that $c_r < 1 - 1/M_\infty$.[3,4,10,11]

The unsteady simulations and LST results in this paper, suggest a different mechanism for the observed acoustic-like waves. The proposed mechanism appears to start with an unstable mode S, which causes the wave packet to grow, likewise mode F is stable, which causes the wave packet to decay. The wave packets trail one another downstream because of there different phase velocities. Dispersion causes the wave packets to spread out. Mode F and S can now interact with one another. Constructive interference causes mode F to grow in the presence of mode S. The growth of mode F causes acoustic-like waves to radiate into the shock layer because of mode F's supersonic phase speed. This is the proposed mechanisms interpreted from the results, moreover the description is a linear process.

It is not clear if this result has any far reaching impact on understanding boundary layer transition. That said, the case in which the downstream actuator, $s_c = 0.2m$, created a disturbance that did not continue to grow downstream due to strong constructive/destructive interference merits further investigation. Moreover, future research should include theoretical work in order to verify or disprove the proposed mechanism. Furthermore, the cause of the primary and satellite wave packets needs investigating. The present investigation suspects it is a consequence of actuator location and its relation to the second mode neutral curve.

In closing this is a peculiar result because the current research holds that the supersonic mode appears on unstable discrete modes in cold wall, high-enthalpy flows—this result challenges that view.

Acknowledgements

This research is sponsored in part by the Air Force Office of Scientific Research (AFOSR) under grant #FA9550-19-1-0206, monitored by Dr. Ivett Leyva, and by the Office of Naval Research (ONR) Grant #N00014-17-1-23-43, monitored by Dr. Eric Marineau. Computational resources were provided by the United States Department of Defense High Performance Computing Modernization Program (DoD HPCMP). The views and conclusions contained herein are those of the authors and should not be interpreted as necessarily representing the official policies or endorsements either expressed or implied of the AFOSR, the ONR, or the U.S. Government.

References

[1]Haley, C. L. and Zhong, X., "Direct Numerical Simulation of Hypersonic Flow over a Blunt Cone with Axisymmetric Isolated Roughness," *47th AIAA Fluid Dynamics Conference*, , No. June, 2017, pp. 1–27.

[2]Knisely, C. P. and Zhong, X., "Significant Supersonic Modes and the Wall Temperature Effect in Hypersonic Boundary Layers," *AIAA J.*, , No. 57(4), 2019, pp. 1552–1566.

[3]Knisely, C. P. and Zhong, X., "Sound radiation by supersonic unstable modes in hypersonic blunt cone boundary layers. I. Linear stability theory," *Physics of Fluids*, , No. 31:024103, 2019.

[4]Knisely, C. P. and Zhong, X., "Sound radiation by supersonic unstable modes in hypersonic blunt cone boundary layers. II. Direct numerical simulation," *Physics of Fluids*, , No. 31:024104, 2019.

[5]Mack, L. M., "Boundary Layer Linear Stability Theory," Tech. rep., AGARD report No. 709, 1984.

[6]Mack, L., "Review of Linear Compressible Stability Theory," *Stability of Time Dependent and Spatially Varying Flows*, edited by D. Dwoyer and M. Hussaini, Springer-Verlag, 1987, pp. 164–187.

[7]Mack, L. M., "On the Inviscid Acoustic-Mode Instability of Supersonic Shear Flows Part 1: Two-Dimensional Waves," *Theoretical Computational Fluid Dynamics*, Vol. 2, 1990, pp. 97–123.

[8]Reshotko, E., "Hypersonic Stability and Transition," *Hypersonic flows for reentry problems*, Vol. 1, No. A93-42576 17-02, 1991, pp. 18–34.

[9]Tumin, A., Private Communication, 2019.

[10]Bitter, N. and Shepherd, J., "Stability of highly cooled hypervelocity boundary layers," *Journal of Fluid Mechanics*, Vol. 778, 2015, pp. 586–620.

[11]Mortensen, C., "Toward and understanding of supersonic modes in boundary-layer transition for hypersonic flow over blunt cones," *J. Fluid Mech*, Vol. 846, 2018, pp. 789–814.

[12]Wu, X. and Zhang, Z., "First-principle description of acoustic radiation of shear flows," *Philosophical Transactions of the Royal Society A: Mathematical, Physical and Engineering Sciences*, Vol. 377, 12 2019, pp. 20190077.

[13]Hollis, B., "Blunt-body entry vehicle aerothermodynamic: transition and turbulent heating," *Journal Spacecraft and Rockets*, Vol. 49, No. 3, 2012, pp. 435–449.

[14]Zhong, X., "High-Order Finite-Difference Schemes for Numerical Simulation of Hypersonic Boundary-Layer Transition," *Journal of Computational Physics*, Vol. 144, No. 2, 1998, pp. 662–709.

[15]Casper, K. M., Beresh, S. J., Henfling, J. F., Spillers, R. W., Pruett, B. O. M., and Schneider, S. P., "Hypersonic Wind-Tunnel Measurements of Boundary-Layer Transition on a Slender Cone," *AIAA Journal*, Vol. 54, No. 4, 2016, pp. 1250–1263.

[16]Fong, K. D., Wang, X., and Zhong, X., "Numerical simulation of roughness effect on the stability of a hypersonic boundary layer," *Computers and Fluids*, Vol. 96, 2014, pp. 350–367.

[17]Huang, Y. and Zhong, X., "Numerical Study of Hypersonic Boundary-Layer Receptivity with Freestream Hotspot Perturbations," *Aiaa J.*, Vol. 52, No. 12, 2014, pp. 1–21.

[18]Lei, J. and Zhong, X., "Linear stability analysis of nose bluntness effects on hypersonic boundary layer transition," *Journal of Spacecraft and Rockets*, Vol. 49, No. 1, 2012, pp. 24–37.

[19]Williamson, J., "Low-Storage Runge-Kutta Schemes," *Journal of Computational Physics*, Vol. 35, No. 1, 1980, pp. 48–56.

[20]Fong, D., Wang, X., and Zhong, X., "Finite roughness effect on modal growth of a hypersonic boundary layer," *50th AIAA Aerospace Sciences Meeting including the New Horizons Forum and Aerospace Exposition*, , No. January, 2012, pp. 1–27.